



<b>Publication Year</b>	2015
<b>Acceptance in OA @INAF</b>	2020-03-25T17:52:38Z
<b>Title</b>	Radial Evolution of Spectral Characteristics of Magnetic Field Fluctuations at Proton Scales
<b>Authors</b>	TELLONI, Daniele; BRUNO, Roberto; Trenchi, L.
<b>DOI</b>	10.1088/0004-637X/805/1/46
<b>Handle</b>	<a href="http://hdl.handle.net/20.500.12386/23572">http://hdl.handle.net/20.500.12386/23572</a>
<b>Journal</b>	THE ASTROPHYSICAL JOURNAL
<b>Number</b>	805

# RADIAL EVOLUTION OF SPECTRAL CHARACTERISTICS OF MAGNETIC FIELD FLUCTUATIONS AT PROTON SCALES

D. TELLONI<sup>1</sup>, R. BRUNO<sup>2</sup>, AND L. TRENCHI<sup>2,3</sup>

<sup>1</sup> National Institute for Astrophysics, Astrophysical Observatory of Torino, Via Osservatorio 20, I-10025 Pino Torinese, Italy

<sup>2</sup> National Institute for Astrophysics, Institute for Space Astrophysics and Planetology, Via del Fosso del Cavaliere 100, I-00133 Roma, Italy

<sup>3</sup> School of Physics & Astronomy, University of Southampton, SO17 1BJ, UK  
Received 2014 December 26; accepted 2015 March 14; published 2015 May 19

## ABSTRACT

This paper addresses the investigation of the character and the radial evolution of magnetic fluctuations within the dissipation range, right after the high-frequency spectral break, employing observations by *Messenger* and *Wind* of the same fast wind stream during a radial alignment. The same event has already been considered in literature to show, for the first time, that the high-frequency break separating the fluid from the kinetic regime moves to lower frequency as the wind expands. The present work aims to analyze the nature of the high-frequency magnetic fluctuations beyond the spectral break and show that their character is compatible with left-hand, outward-propagating, ion cyclotron waves and right-hand kinetic Alfvén waves. It is also shown that the low-frequency limit of these fluctuations follows the radial evolution of the spectral break, which also reflects in the behavior of their intermittency character. Finally, the total power and the compressive character of these two wave populations are analyzed and compared as a function of the heliocentric distance, leading us to conclude that the overall picture is in favor of a radial decrease.

*Key words:* interplanetary medium – magnetic fields – plasmas – solar wind – turbulence – waves

## 1. INTRODUCTION

Recently, several authors focused on the frequency location of the spectral break between fluid and kinetic regimes in the solar wind magnetic fluctuations (see review by Alexandrova et al. 2013). The frequency break ( $f_b$ , hereafter) could be associated with one of these two characteristic lengths: the proton inertial length,  $\lambda_i = c/\omega_p$ , or the proton Larmor radius,  $\lambda_L = v_{th}/\Omega_p$ , expressed in cgs units. In the above expressions  $\omega_p = (4\pi nq^2/m_p)^{1/2}$  and  $\Omega_p = qB/(m_p c)$  are the plasma and cyclotron frequencies, respectively, and  $q$ ,  $n$ ,  $B$ ,  $m_p$ ,  $c$ , and  $v_{th}$  are the proton electric charge, the proton number density, the local magnetic field intensity, the proton rest mass, the speed of light, and the thermal speed, respectively. Moreover, since  $c/\omega_p = v_A/\Omega_p$ , where  $v_A = B/(4\pi nm_p)^{1/2}$  is the Alfvén speed, the proton inertial length can also be expressed as  $\lambda_i = v_A/\Omega_p$ . Each of these two lengths assumes a relevant role depending on the dissipation mechanism invoked to explain the observed local heating of the solar wind plasma during expansion within fast wind (Marsch 2012), but the spectral break is observed to be always at scales slightly larger than both  $\lambda_i$  and  $\lambda_L$ . For Dmitruk et al. (2004) the role of  $\lambda_i$  becomes relevant for 2D turbulence dissipation via turbulence reconnection processes and generation of current sheets of the order of  $\lambda_i$  itself. On the other hand, Leamon et al. (1998) showed that  $\lambda_L$  can be invoked for damping kinetic Alfvén waves (KAWs), propagating at large angles with respect to the local mean magnetic field. However, Galtier (2006) showed that there is no need to invoke dissipation at proton scales since  $\lambda_i$  can be associated with another process that is able to steepen the spectrum as well: the Hall effect. Further investigations, based on in situ observations, tried to associate the spectral location of the break with the above proton scales and also verify whether the break position was related to the local plasma conditions.

Markovskii et al. (2008), based on *ACE* observations at 1 AU, concluded that none of the available models were able to

reproduce the exact location of the break and suggested that it is likely due to a combination of the scale of the turbulent fluctuations and their amplitude at that scale.

Sahraoui et al. (2009), using *Cluster* observations in the solar wind, showed that turbulence made of highly oblique KAWs could account for the observed turbulence cascade below the proton gyroscale  $\lambda_L$  and its dissipation at the electron gyroscale via collisionless electron Landau damping.

Perri et al. (2010) mostly focused on the radial evolution of the position of the frequency break  $f_b$ . These authors analyzed several data intervals distributed between 0.3 and 5 AU. They employed *Messenger* and *Ulysses* measurements in the inner and outer heliosphere, respectively, though they could not determine the solar wind conditions for the inner heliosphere since plasma observations were not available from *Messenger*. These authors concluded that the observed value of  $f_b$  seems to be independent of the distance from the Sun and thus of the Doppler-shifted ion-cyclotron frequency and of the frequencies corresponding to the proton inertial length  $\lambda_i$  and to the proton Larmor radius  $\lambda_L$ .

Similar conclusions were drawn by Bourouaine et al. (2012), who analyzed *Helios* magnetic field spectra between 0.3 and 0.9 AU. However, these authors found a partial agreement between the spatial scale corresponding to  $f_b$  and the proton inertial scale  $\lambda_i$  rather than the proton gyroscale  $\lambda_L$ , under the assumption of dominant 2D turbulence.

Recently, Bruno & Trenchi (2014) studied the radial evolution of the  $f_b$  location between 0.42 and 5.3 AU, analyzing radial alignments between *Messenger* and *Wind* for the inner heliosphere and between *Wind* and *Ulysses* for the outer heliosphere. These authors proved, for the first time in literature, that the spectral break separating the inertial from the dissipation range moves to lower frequency as the wind expands, finding a well-established radial dependence of  $f_b$  of the kind  $\sim R^{-1.09}$ . Moreover, the wavenumber associated with  $f_b$  was always in a better agreement with the wavenumber  $\kappa_r$ ,

corresponding to the resonance condition for parallel-propagating Alfvén waves rather than with the wavenumbers associated with  $\lambda_i$  and  $\lambda_L$ .

On the other hand, authors like He et al. (2011, 2012a, 2012b) and Podesta & Gary (2011), among others, studied the nature of the fluctuations that populate the proton scales near  $f_b$ , looking at their polarization state on a plane perpendicular to the sampling direction and for different pitch angles with respect to the local mean magnetic field orientation, following the technique first suggested by Horbury et al. (2008). In particular, He et al. (2011), using *STEREO* measurements, found the possible simultaneous signatures of right-handed polarized KAWs (or whistler waves) at large angles with the local mean magnetic field  $B_0$  and left-handed Alfvén/ion-cyclotron waves outward propagating quasi-(anti-)parallel to  $B_0$ . This result was confirmed later by Podesta & Gary (2011) by using *Ulysses* observations. The same authors also suggested that the left-hand magnetic polarization for the outward-propagating Alfvén/ion-cyclotron waves could also be related to inward-propagating whistler waves in the case of a field-aligned drift instability.

Previous inferences of the presence of KAWs were obtained by Goldstein et al. (1994), Leamon et al. (1998), and Hamilton et al. (2008), but the Fourier analysis they used did not allow them to unravel the presence of left-handed polarized Alfvén/ion-cyclotron waves. On the other hand, the data analysis technique employed by He et al. (2011) and Podesta & Gary (2011), which will be described in the following, is based on the wavelet transform of the normalized magnetic helicity (Matthaeus & Goldstein 1982), introduced for the first time by Bruno et al. (2008).

In this paper, as a continuation of the results reported in the companion paper by Bruno & Trenchi (2014), the radial evolution of the magnetic field fluctuations beyond the frequency break is investigated, in terms of their magnetic polarization, compression, and intermittency, analyzing measurements of the same fast-wind plasma observed by the *Messenger* and *Wind* spacecraft during one of the radial alignments previously studied in Bruno & Trenchi (2014).

## 2. DATA ANALYSIS

The study of the radial evolution of the interplanetary magnetic fluctuations at proton scales is performed by analyzing *Messenger* and *Wind* high-resolution data acquired from 2010 June 29 to July 16, when the two spacecraft were radially aligned. Magnetic field measurements in the inner heliosphere were performed by the magnetometer (MAG; Anderson et al. 2007) on board *Messenger*, at 20 Hz, and by the Magnetic Field Instrument (MFI; Lepping et al. 1995) on board *Wind*, at about 11 Hz.

During the radial alignment, *Messenger* was cruising toward Mercury at 0.56 AU from the Sun. The same fast stream observed by *Messenger* around July 1 reached *Wind* orbiting around L1 at 0.99 AU approximately a day and half later (Bruno & Trenchi 2014). It is worth noting that, since plasma parameters from *Messenger* are not available, the correspondence between the time intervals when the same high-speed stream crosses the two spacecraft was found by taking into account the transit time from 0.56 to 0.99 AU (using an average wind speed of  $604 \text{ km s}^{-1}$  as measured by *Wind*) and by identifying similar magnetic field structures observed by both spacecraft.

As described in the following, the spectral analysis of the magnetic field fluctuations is based on specific tools like the normalized magnetic helicity spectrum and the power spectra of compressive and directional fluctuations computed using wavelet techniques and examined in terms of the angle between the solar wind velocity and the local mean magnetic field orientation  $\theta_{VB}$ .

### 2.1. Angle Distribution of the Magnetic Helicity

The normalized reduced magnetic helicity  $\sigma_m$  can be investigated in both time  $t$  and temporal scale  $\tau$  by means of the wavelet transforms (Torrence & Compo 1998). According to Matthaeus et al. (1982), the time distribution of  $\sigma_m(t, \tau)$  can be expressed as

$$\sigma_m(t, \tau) = \frac{2 \operatorname{Im}[W_y^*(t, \tau) \cdot W_z(t, \tau)]}{|W_y(t, \tau)|^2 + |W_z(t, \tau)|^2}, \quad (1)$$

where  $W_y(t, \tau)$  and  $W_z(t, \tau)$  are the complex Paul-wavelet transforms of the  $y$  and  $z$  components of the magnetic field and the asterisk indicates the complex conjugate (it is worth reminding that the scale  $\tau$  is related to the Paul-wavelet scale  $s$  by  $\tau = 1.4s$ ). The normalized quantity  $\sigma_m(t, \tau)$  can vary between  $-1$  and  $+1$ , for *left* or right circular polarization (for an outward orientation of the background magnetic field), and indicates which one dominates at a given time and scale.

In order to redistribute  $\sigma_m$  from a time distribution to a  $\theta_{VB}$  distribution, it is first required to determine the time variation at various scales of the angle between the magnetic field and the flow direction of the solar wind, considered radial,  $\theta_{VB}(t, \tau) = \arccos(\hat{\mathbf{R}} \cdot \mathbf{B}_0(t, \tau)/|\mathbf{B}_0(t, \tau)|)$ , and therefore to estimate the local mean magnetic field  $\mathbf{B}_0(t, \tau)$  at any given time  $t$  and scale  $\tau$ . This is defined as the convolution between the instantaneous magnetic field  $\mathbf{B}_0(t)$  and a Gaussian function (normalized to unity) whose width is the scale of interest  $\tau$  (Horbury et al. 2008; He et al. 2011; Podesta & Gary 2011):

$$\mathbf{B}_0(t, \tau) = \int \frac{1}{\sqrt{2\pi}\tau} \exp\left[-\frac{(t-x)^2}{2\tau^2}\right] \mathbf{B}(x) dx. \quad (2)$$

The angle distribution of the normalized magnetic helicity in the interval  $\theta_a < \theta_{VB} < \theta_b$  is thus derived averaging, scale by scale, the values of  $\sigma_m(t, \tau)$  corresponding to those times  $t$  for which the local mean magnetic field forms an angle with the solar wind velocity ranging between  $\theta_a$  and  $\theta_b$ . The  $\theta_{VB}$  distribution of the magnetic helicity is obtained with an angular resolution of  $1^\circ$ .

### 2.2. Significance Level of the Angle Distribution of the Magnetic Helicity

To determine the significance level for the angle distribution of  $\sigma_m$ , one first needs to choose an appropriate background distribution. It is then assumed that different realizations of the physical process (namely, the identification of magnetic helicity features at quasi-perpendicular and quasi-parallel directions in the dissipative range—signatures for kinetic Alfvén or whistler waves and Alfvén/ion-cyclotron waves, respectively; He et al. 2011; Podesta & Gary 2011) will be randomly distributed about the expected background. The observed angle distribution of the magnetic helicity can be compared against this random distribution. This background is

indeed used to establish a null hypothesis for the significance of a feature in the  $\sigma_m$  distribution as a function of  $\theta_{VB}$ .

The background for the angle distribution of  $\sigma_m$  can be obtained from the observed data by randomizing the phase of the  $y$ - and  $z$ -components of the magnetic field, in such a way to construct a magnetic helicity wavelet spectrum randomly fluctuating around the null helicity. In order to do so, the amplitudes of both  $B_y$  and  $B_z$  are first calculated via the Fourier transform, and the relative phases are randomized.

Successively, using the inverse transform, the uncorrelated time series of  $B_y$  and  $B_z$  are obtained. The original and the synthetic non-correlated data obviously share the same Fourier power spectrum, but while peaks in the magnetic helicity wavelet spectrum inferred from the observed data might be due to correlated rotations of the magnetic field components, those exhibited in the wavelet spectrum obtained from the uncorrelated data are certainly due to Gaussian random noise. By computing the angle between the solar wind velocity and the synthetic uncorrelated local magnetic field, it is then possible to construct the angle distribution of the background magnetic helicity. Hence, by comparing the (local) spectra of the normalized magnetic helicity observed at every angle  $\theta_{VB}$  with the background wavelet spectrum averaged over the whole range of angles (that is,  $[0^\circ-180^\circ]$ ), it is possible to identify the magnetic helicity features above the expected background spectrum.

As a null hypothesis it is assumed that the mean background spectrum at a certain  $\theta_{VB}$  is given by the angle average of the magnetic helicity distribution obtained from the uncorrelated  $B_y$  and  $B_z$  time series. If a feature in the magnetic helicity spectrum at the same angle is significantly above this background spectrum, then it can be assumed to be a true feature with a certain percent confidence. Saying ‘‘significant at the 1% level’’ is equivalent to indicating ‘‘the 99% confidence level,’’ and it implies a test against a certain background level.

The wavelet spectrum of a normally distributed random variable is chi-square distributed with two degrees of freedom (DOFs), denoted by  $\chi_2^2$  (Jenkins & Watts 1968). Thus, also the angle distribution of the magnetic helicity is expected to be  $\chi_2^2$  distributed. To determine the 99% confidence level (significant at 1%) for the magnetic helicity distribution, one multiplies the background distribution by the 99th percentile value for  $\chi_2^2$  (Gilman et al. 1963).

### 2.3. Angle Distribution of the Magnetic Energy Spectra

Similarly to what has been done for the magnetic helicity, the  $\theta_{VB}$  distribution of the power of the compressive and directional components of the magnetic field fluctuations can be obtained from the Paul-wavelet transforms of the components of the magnetic field vector. In particular, the wavelet transform of the intensity of the magnetic field vector  $|W_B(t, \tau)|^2$  quantifies the power of compressive fluctuations, while the trace  $E_B(t, \tau)$  of the spectral matrix, that is, the sum of the wavelet spectra of the three orthogonal  $xyz$  components of the magnetic field vector,  $E_B(t, \tau) = |W_x(t, \tau)|^2 + |W_y(t, \tau)|^2 + |W_z(t, \tau)|^2$ , provides information on the total power of the magnetic field fluctuations (Bruno & Bavassano 1991). Hence, the angle distribution of the power corresponding to the compressive and directional components of the magnetic fluctuations in the interval  $\theta_a < \theta_{VB} < \theta_b$  is obtained averaging, scale by scale,

the power values at those times  $t$  for which the angle between the local magnetic field and the wind direction ranges between  $\theta_a$  and  $\theta_b$ .

The ratio between the angle distributions of the power of the compressive and directional fluctuations yields the angle distribution of the compressibility of the magnetic fluctuations; indeed, a compression ratio close to 0 is indicative of fluctuations dominated by changes in the vector orientation, while a value close to 1 suggests that the intensity fluctuations are dominant.

The power spectrum of the magnetic field fluctuations exhibits three different spectral regimes, corresponding to the so-called injection, inertial, and dissipative ranges, where the power density drops off as  $\sim k^\alpha$  (see Tu & Marsch 1995; Bruno & Carbone 2013, and references therein) and  $\alpha$  assumes values of  $-1$ ,  $-5/3$ , and generally larger than  $-2$ , respectively. Hence, especially at the proton scales, any possible feature in the angle distribution of the power spectra of the compressive and directional components of the magnetic fluctuations is dominated by the largest scales in that specific frequency range. Consequently, in order to highlight localized structures at any frequency, the wavelet spectrum has to be compensated in such a way to level out the associated power throughout the whole spectral band, before deriving its angular distribution. This is done by dividing the square of the wavelet coefficients at a given scale by their average value computed throughout the time interval.

## 3. RESULTS

The total magnetic power spectra shown in Figure 1 have been adapted from the left panel of Figure 29 of Bruno & Carbone (2013) and from Figure 2 of Bruno & Trenchi (2014) and show, for the first time in literature, the radial dependence of the spectral locations of the low- and high-frequency breaks. All the spectra have been derived from magnetic field fluctuations within fast wind observed in the ecliptic plane. In particular, the spectra at 0.29, 0.65, and 0.89 AU refer to *Helios 2* measurements of the same co-rotating fast-wind stream recorded by the spacecraft during its first solar mission in 1976, at three successive solar rotations. The power spectral densities at 1.4 AU correspond to two time intervals within the same stream observed by *Ulysses* at the end of August of 2007. The spectrum at 0.42 AU refers to *Messenger* measurements between 2011 April 10 and 11, while the one relative to 0.56 AU corresponds to *Messenger* observations performed during 2010 July 1. In particular, this last interval, which refers to a radial alignment event between *Messenger* and *Wind*, and the corresponding *Wind* time interval taken at 1 AU about 36 hr later lend themselves as particularly apt to be studied in terms of radial evolution of magnetic fluctuations at proton scales. Finally, the overall radial excursion presented in Figure 1 ranges between 0.29 and 1.4 AU at low frequencies and between 0.42 and 1.4 AU at higher frequencies.

Both the low- and the high-frequency spectral breaks move to lower and lower frequencies as the wind expands. However, the radial dependence of the two breaks is quite different, with the low-frequency one having a faster radial evolution. In particular, while the radial dependence of the low-frequency break is governed by a power law of the order of  $R^{-1.5}$  (Bruno & Carbone 2013), the one separating the fluid from the kinetic regime drops off as  $R^{-1.1}$  (Bruno & Trenchi 2014); therefore, the inertial range grows with increasing heliocentric distance.

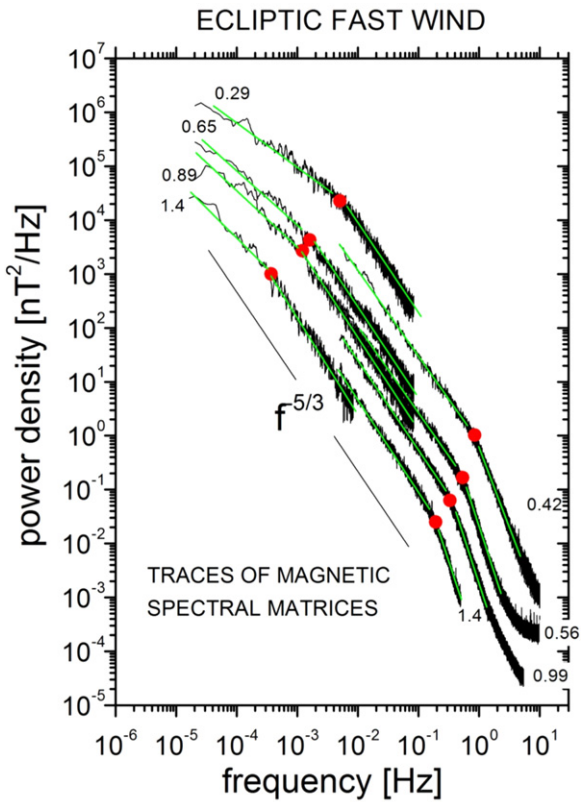


**Figure 1.** Magnetic field spectral densities relative to measurements recorded by *Messenger* (at 0.42 and 0.56 AU), *Helios 2* (at 0.29, 0.65 and 0.89 AU), *Wind* at the Lagrangian point L1, and *Ulysses* at 1.4 AU within high-speed streams observed in the ecliptic. Low- and high-frequency breaks are both marked by red dots. The solid line shows, for reference, the Kolmogorov-like spectral slope ( $f^{-5/3}$ ). Image adapted from Bruno & Carbone (2013) and Bruno & Trenchi (2014).

At this point it is interesting to look at the evolution, if any, of the magnetic field fluctuations around and beyond the frequency break delimiting the dissipation range, by studying, as already said, the alignment experienced by *Messenger* and *Wind* in 2010 July when *Messenger* was at about 0.56 AU from the Sun.

The results obtained from the analysis of the polarization of the magnetic field fluctuations are presented in Figure 2, which shows the distribution of the normalized magnetic helicity with respect to the local field pitch angle at the *Messenger* (left panel) and *Wind* (right panel) distances. The frequencies corresponding to the proton inertial length,  $f_i$ , the proton Larmor radius,  $f_L$ , the observed spectral break,  $f_b$ , and the resonance condition for parallel-propagating Alfvén waves,  $f_r$  (Leamon et al. 1998; Bruno & Trenchi 2014), are shown for the two distances as horizontal solid, dotted, dashed, and dotted-dashed lines, respectively.

The results are qualitatively similar to those reported by He et al. (2011) and Podesta & Gary (2011) since, also in this case, the background magnetic field is characterized by an inward orientation. These results are generally obtained whenever the time interval is long enough to extend the analysis at frequencies well below the spectral break, but short enough to provide a magnetic polarity reasonably steady (see various examples shown by He et al. 2011). However, the actual range of the local field pitch angles covered by the observations strictly depends on the magnetic field orientation; hence, while in the case of the *Messenger* measurements the angle between the magnetic field and the flow direction of the solar wind spans the whole range of angles between  $0^\circ$  and  $180^\circ$ , in the case of the *Wind* data the inclination of the local mean magnetic field with respect to the solar wind velocity is never lower than  $45^\circ$ . The  $\sigma_m$  angular distribution shows, for both *Messenger* and *Wind* observations, two dominant excesses of magnetic helicity (of opposite polarity) at quasi-perpendicular and quasi-parallel directions around the Doppler shifted ion-cyclotron frequency, which are to be tested for significance or randomness, following the procedure described in Section 2.2. The black lines show the 99% confidence level, which implies that there is only a probability of 1% that results encircled by the 99% contours can be obtained by chance.

Both features of opposite helicity at  $\sim 90^\circ$  and  $\sim 180^\circ$ , observed at *Messenger* and *Wind* distances, are above the 99% confidence level, which implies that they correspond to a real underlying physical process. At odds, the positive magnetic helicity patch observed by *Messenger* at pitch angles of  $\sim 20^\circ$  with respect to the local mean magnetic field orientation is not encircled by the 99% confidence level and, in turn, has only a

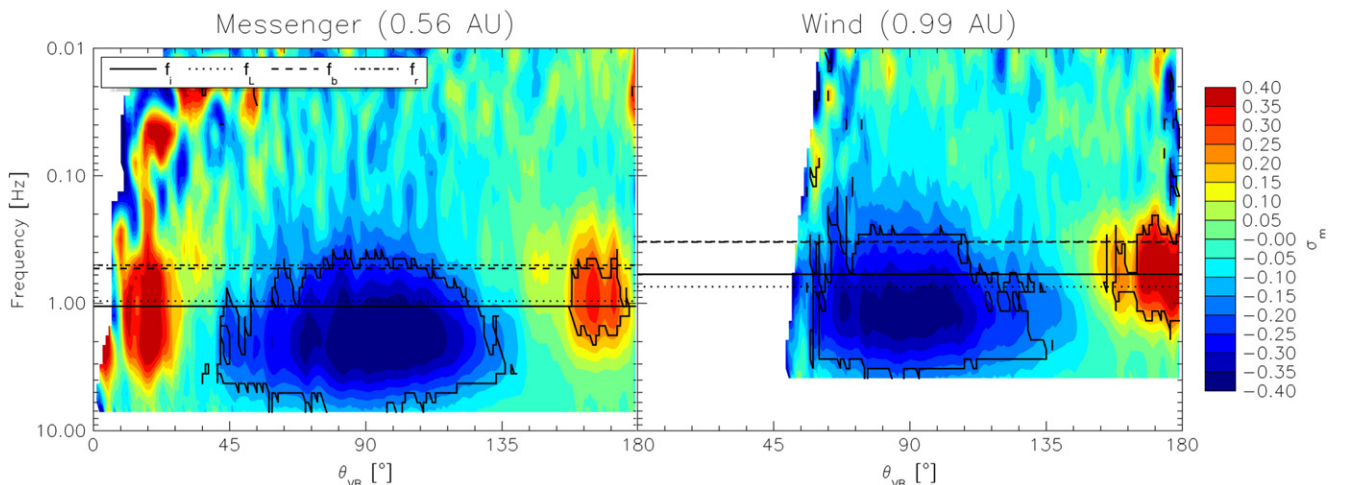


**Figure 2.** Distribution of the normalized magnetic helicity spectrum as a function of the pitch angle  $\theta_{VB}$  between the local mean magnetic field and the flow direction, observed during the radial alignment between the *Messenger* and *Wind* spacecraft, at 0.56 AU (left) and 0.99 AU (right). The black lines show the 99% confidence levels. The horizontal solid, dotted, dashed and dotted-dashed lines represent the frequencies corresponding to the proton inertial length  $f_i$ , the proton Larmor radius  $f_L$ , the observed spectral break  $f_b$ , and the resonance condition for parallel-propagating Alfvén waves  $f_r$ , respectively.

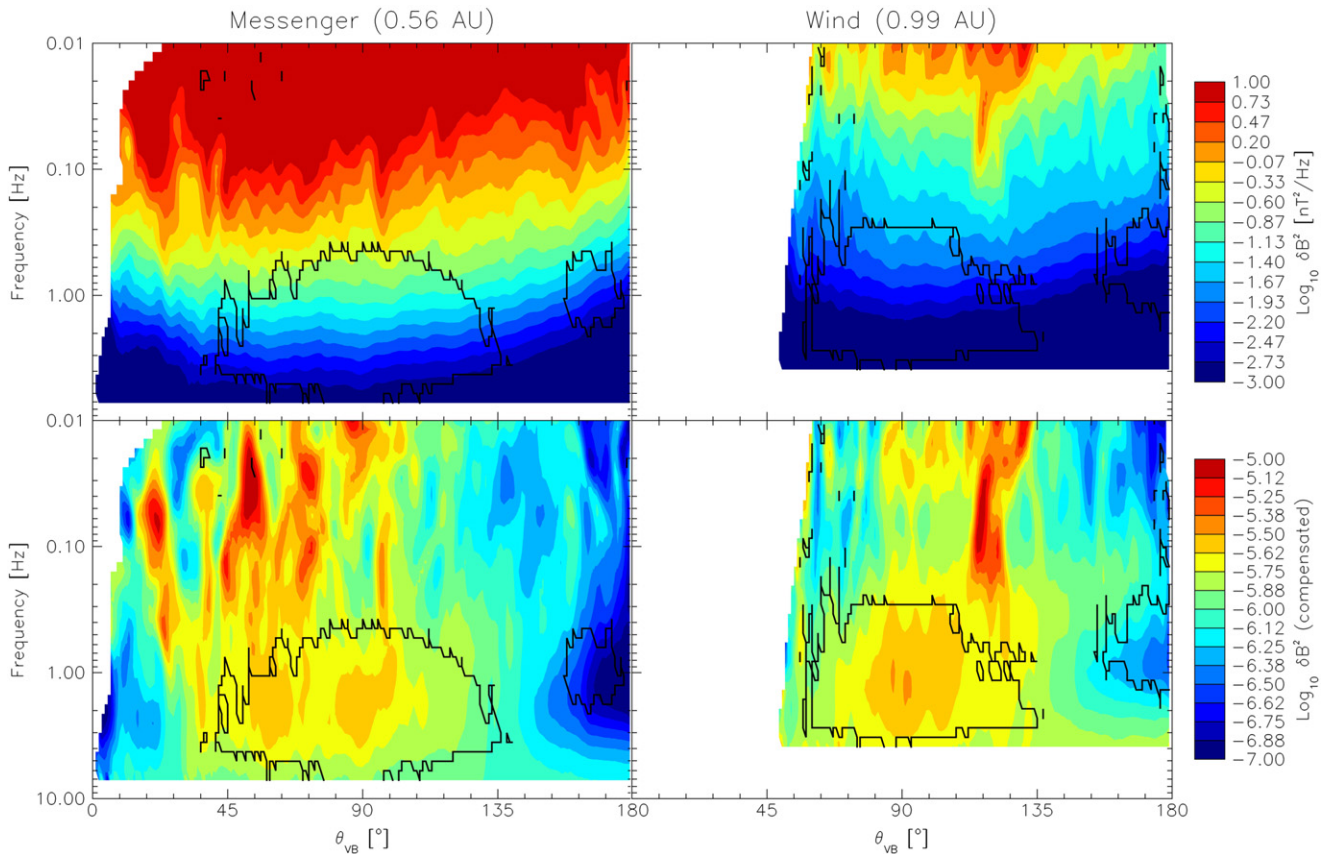


**Figure 3.** Distribution of the power spectrum of the compressive component of the magnetic fluctuations as a function of the angle  $\theta_{VB}$  between the local mean magnetic field and the flow direction, observed during the radial alignment between the *Messenger* and *Wind* spacecraft, at 0.56 AU (left panels) and 0.99 AU (right panels), before (upper panels) and after (lower panels) the compensation procedure (see text for details). The black lines represent the 99% confidence levels for the angle distribution of the normalized magnetic helicity (Figure 2).

probability of 1% not to be due to noise. Thus, the existence of two populations of right- and left-handed polarized magnetic fluctuations (the magnetic sector is inward oriented, thus positive [negative] magnetic helicity corresponds to left [right] circular polarization), propagating, respectively, highly obliquely and quasi-antiparallel with respect to  $B_0$ , are significantly resolved. Quite interestingly, both populations shift toward lower frequencies when observed at 1 AU and the frequency break is located around the lower frequency extent of the two populations rather than around their respective peaks. On the contrary, the frequencies related to the proton inertial length  $f_i$  and Larmor radius  $f_L$ , which are rather close to each other, are shifted toward the core of the two populations.

Magnetic fluctuations with negative helicity seem to dominate (being wider in both scales and angles) on the left-handed polarized component, producing a net total magnetic helicity signature (He et al. 2011). In order to quantify this aspect, it is necessary to evaluate the power associated with both populations in terms of compressive and directional fluctuation contributions. The upper panels of Figure 3 show the angular distributions of the power spectrum of the intensity of the magnetic field vector, say, of the compressive component of the magnetic field fluctuations, at the *Messenger* (left panel) and *Wind* (right panel) distances. The lower panels of the same figure show instead the angle distributions of the compressive power spectrum leveled out throughout the frequency range, by means of the compensation procedure

described in Section 2.3 and aimed to highlight possible structures at any frequency.

The results reported in the upper panels show a lower level of fluctuations around parallel and antiparallel directions and do not allow us to recognize the two populations clearly shown in Figure 2. Indeed, due to the spectral steepness, the power associated with lower-frequency fluctuations largely dominates and does not allow us to resolve structures at higher frequencies. On the other hand, the result of the compensation performed on the spectrum before deriving the angular distribution (shown in the lower panels of Figure 3) does allow the identification of right-handed quasi-perpendicular and left-handed quasi-antiparallel fluctuations as shown in Figure 2. Field intensity fluctuations around  $\theta_{VB} \sim 90^\circ$  are largely more compressive than those around  $180^\circ$  for both data samples at 0.56 and 0.99 AU. In particular, it is possible to give an estimate of the power ratio between fluctuations associated with the right- and left-handed polarized populations, integrating the angle distribution of the power spectrum within the 99% confidence level contours. Obviously, this integration is performed before any spectral compensation. In this way, it is possible to compare the power associated with the quasi-perpendicular and quasi-parallel fluctuations taking into account the caveat that the analysis based on the reduced magnetic helicity might not detect all the available fluctuations, especially those propagating highly obliquely to the local magnetic field, being more sensitive to waves propagating along the radial direction. For *Messenger*, at 0.56 AU, the

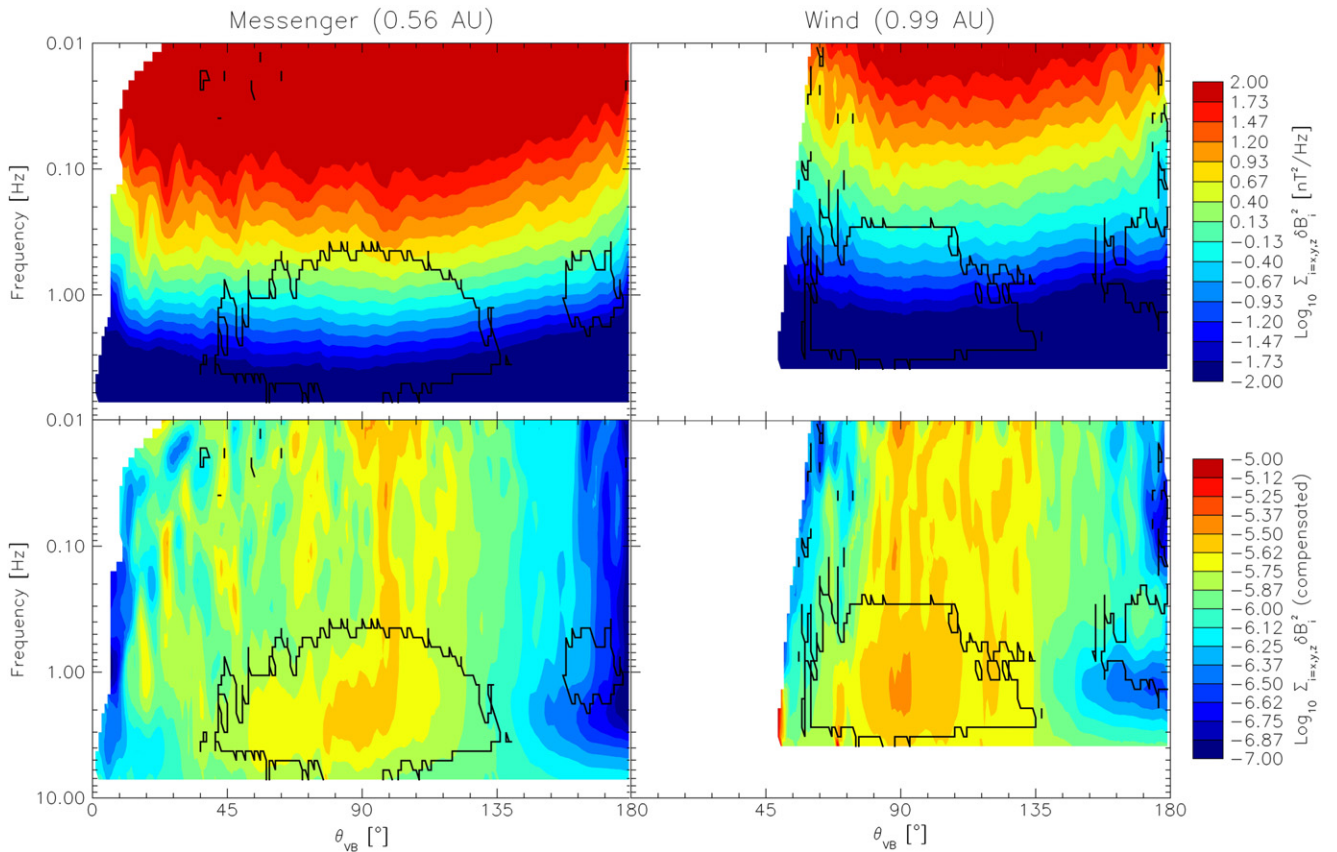


**Figure 4.** Distribution of the power spectrum of the directional component of the magnetic fluctuations as a function of the angle  $\theta_{VB}$  between the local mean magnetic field and the flow direction, observed during the radial alignment between the *Messenger* and *Wind* spacecraft, at 0.56 AU (left panels) and 0.99 AU (right panels), before (upper panels) and after (lower panels) the compensation procedure (see text for details). The black lines represent the 99% confidence levels for the angle distribution of the normalized magnetic helicity (Figure 2).

power level corresponding to the right- and left-handed polarized populations, normalized to their extent in the frequency-angle space, are  $1.06 \times 10^{-1} nT^2$  and  $1.16 \times 10^{-2} nT^2$ , respectively. At 0.99 AU, *Wind* shows values around  $8.56 \times 10^{-3} nT^2$  and  $1.87 \times 10^{-3} nT^2$  for the quasi-perpendicular and quasi-parallel population, respectively. Thus, not only the power of the compressive component of both the quasi-perpendicular and quasi-parallel fluctuations decreases with the heliocentric distance, but also the ratio between these estimates decreases from about 9.1 at 0.56 AU to about 4.6 at 0.99 AU, showing that compressive phenomena due to perpendicular fluctuations always dominate on the parallel counterpart, although this effect seems to decrease with distance.

A similar analysis has been performed for the directional fluctuations of the magnetic field vector. The results are reported in Figure 4, which shows the angle distributions of the total magnetic energy spectrum at *Messenger* (left panels) and *Wind* (right panels) distances, derived before and after the leveling out of the associated power using the spectral compensation (upper and lower panels, respectively).

Also in this case the spectral compensation allows us to localize the two different populations. Integrals of the angle distribution of the total power spectrum performed within the 99% confidence level contours, and normalized to the spectral and angular extent of the corresponding populations, provide the following values: at 0.56 (0.99) AU, *Messenger* (*Wind*) shows power levels of  $1.12 nT^2$  ( $1.32 \times 10^{-1} nT^2$ ) and

$2.53 \times 10^{-1} nT^2$  ( $4.34 \times 10^{-2} nT^2$ ) for the magnetic fluctuations sampled at quasi-perpendicular and quasi-parallel directions, respectively. The total power associated with both populations decreases with increasing heliocentric distance, as well as the ratio between these estimates, which is around 4.4 at 0.56 AU and around 3.0 at 0.99 AU. However, quite interestingly, this ratio is lower than that derived between the power levels associated solely with the compressive fluctuation component and, moreover, decreases more slowly with the heliocentric distance, indicating that, at odds with the perpendicular counterpart, parallel population is dominated by directional rather than compressive fluctuations.

In terms of compressibility, expressed as the ratio between the power associated with intensity fluctuations and the total magnetic energy (Bavassano et al. 1982), a slight decrease from 9.4% at 0.56 AU to 6.5% at 0.99 AU is observed for the quasi-perpendicular fluctuations, while the quasi-parallel counterpart keeps a lower compressibility level of about 4.3%–4.6% during the wind expansion. It turns out that, since the quasi-perpendicular population energetically dominates on the quasi-parallel one, the overall picture records a slight decrease of compressibility with radial distance. This appears evident in Figure 5, which shows the angle distributions of the compression ratio, at the *Messenger* (left panel) and *Wind* (right panel) distances, computed as the ratios between the angular distributions of the power spectrum of the magnetic field magnitude (upper panels of Figure 3) and total magnetic energy spectrum (upper panels of Figure 4).

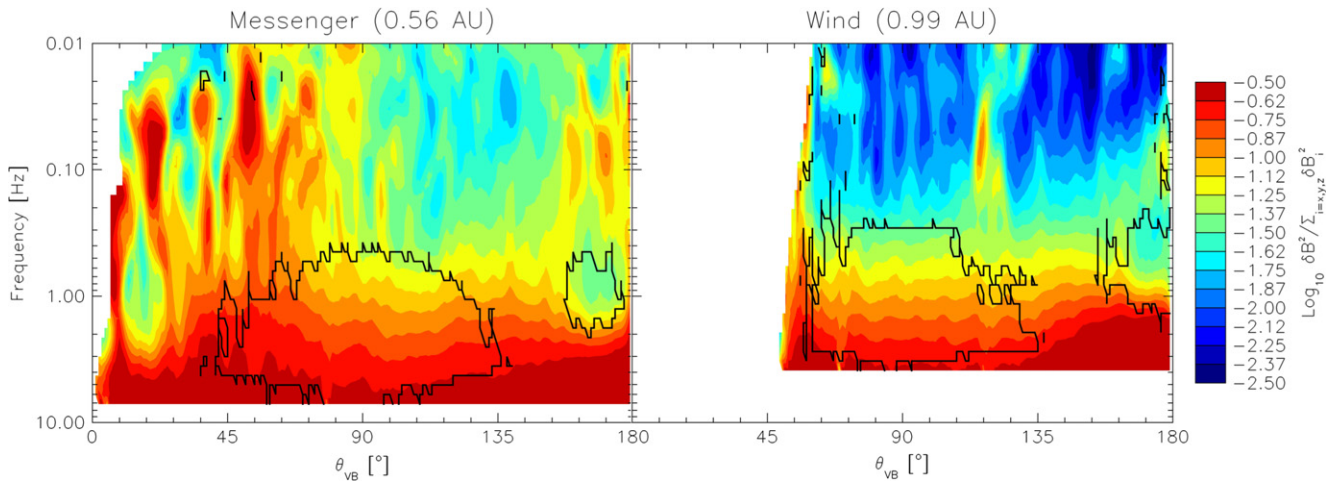


**Figure 5.** Distribution of the compression ratio as a function of the angle  $\theta_{vB}$  between the local mean magnetic field and the flow direction, observed during the radial alignment between the *Messenger* and *Wind* spacecraft, at 0.56 AU (left) and 0.99 AU (right). The black lines represent the 99% confidence levels for the angle distribution of the normalized magnetic helicity (Figure 2).

Higher values of compressibility are indeed clearly visible within the 99% confidence level contour for magnetic fluctuations at angles centered about the perpendicular direction, with respect to those found in the structure corresponding to left-handed polarized magnetic fluctuations located at quasi-parallel direction, which is largely recovered without any spectral compensation also in this figure.

Finally, following previous analyses related to the intermittent character of the fluctuations within the frequency range of interest, it is possible to look also at the radial evolution of the intermittency level of the magnetic fluctuations moving across the high-frequency spectral break. This was done by estimating the value of the flatness of the magnetic field intensity from the smallest scale (corresponding to the Nyquist frequency) up to scales of about 5 hr, which are known to be characterized by rather Gaussian fluctuations. The reader is referred to Bruno et al. (2003, 2014) for rather exhaustive details on the analysis methodology based on the flatness and for a review on previous intermittency results achieved for magnetic and velocity field, and density, fluctuations throughout the inner heliosphere, within both fast and slow wind. Results relative to the intermittency analysis are reported in Figure 6 for both *Messenger* (blue dots) and *Wind* (red dots) data. The frequencies corresponding to the proton inertial length,  $f_i$ , the proton Larmor radius,  $f_L$ , the observed spectral break,  $f_b$ , and the resonance condition for parallel-propagating Alfvén waves,  $f_r$ , are shown at the *Messenger* (blue lines) and *Wind* (red lines) distances as vertical solid, dotted, dashed, and dotted–dashed lines, respectively.

At both heliocentric distances the flatness increases when considering frequencies higher than about  $10^{-3}$  Hz up to frequencies of the order of  $10^{-1}$  Hz, unraveling the intermittent character of the magnetic fluctuations. However, since at the *Wind* distance the flatness grows more rapidly, reaching larger values at higher frequencies (red dots in Figure 6), magnetic fluctuations at 0.99 AU can be considered more intermittent than those at 0.56 AU, indicating that intermittency increases during the wind expansion. This is a well-known result widely reported in literature (e.g., Bruno et al. 2003), though previous papers focused on the inertial range, up to frequencies of about  $10^{-2}$  Hz. However, both curves exhibit a maximum that moves

at lower frequencies as the heliocentric distance increases but, in both cases, slightly before the corresponding high-frequency breaks  $f_b$  (vertical dashed lines in Figure 6). At higher frequencies the flatness drops off, reaching values typical of the Gaussian fluctuations around 10 Hz. A clear decrease of the flatness right after the high-frequency break has already been reported in literature (e.g., Wu et al. 2013), but this is the first time that it is shown that this decrease roughly coincides with the lowest-frequency extension of the right- and left-handed polarized populations identified in Figure 2, which is at slightly lower frequency compared to the frequency break.

#### 4. SUMMARY AND DISCUSSION

The different radial dependence estimated for the low- and high-frequency spectral breaks and the consequent growth of the inertial range prove what has been several times suggested in literature, namely, that the turbulence in the high-speed plasma is evolving during the wind expansion (see Tu & Marsch 1995; Bruno & Carbone 2013, and references therein).

The low- and high-frequency breaks are strictly related to the correlation length  $\lambda_C$  and the Taylor scale  $\lambda_T$ , respectively, which can be used to determine empirically the effective magnetic Reynolds number  $R_m^{\text{eff}}$  as (Matthaeus et al. 2005)

$$R_m^{\text{eff}} = \left( \frac{\lambda_C}{\lambda_T} \right)^2. \quad (3)$$

The correlation length  $\lambda_C$  represents the largest separation distance over which eddies are still correlated, that is, the largest turbulent eddy size, and marks de facto the transition from the injection to the inertial range. Hence, it is related, through the Taylor hypothesis (Taylor 1938), to the low-frequency break  $f_{b,\text{low}}$ , i.e.,  $\lambda_C \approx V_{\text{sw}}/f_{b,\text{low}}$ , where  $V_{\text{sw}}$  is the solar wind speed. On the other hand, the Taylor scale  $\lambda_T$  is the scale size at which viscous dissipation begins to affect the eddies and separates the fluid from the kinetic regime, being thus related to the high-frequency break  $f_{b,\text{high}}$  via  $\lambda_T \approx V_{\text{sw}}/f_{b,\text{high}}$ . This suggests to evaluate, although roughly, the effective magnetic Reynolds number as the square of the

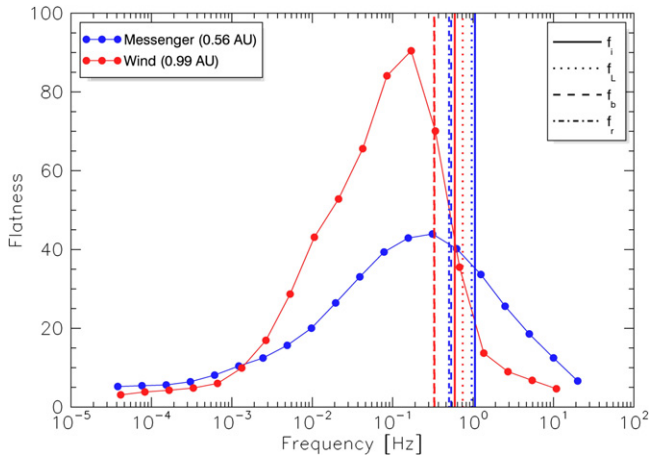


**Figure 6.** Flatness as a function of frequency, relative to intensity fluctuations of the magnetic field observed, within the same fast-wind stream, at 0.56 AU (blue dots) and 0.99 AU (red dots), by the *Messenger* and *Wind* spacecraft, respectively. The vertical solid, dotted, dashed, and dotted-dashed lines represent the frequencies corresponding to the proton inertial length,  $f_i$ , the proton Larmor radius,  $f_L$ , the observed spectral break,  $f_b$ , and the resonance condition for parallel-propagating Alfvén waves,  $f_r$ , respectively.

ratio between the high- and low-frequency spectral breaks, whose values can be inferred from Figure 2, thus obtaining the following values for  $R_m^{\text{eff}}$  at different heliocentric distances:  $3 \times 10^4$  at about 0.35 AU,  $1.1 \times 10^5$  at about 0.65 AU,  $1.5 \times 10^5$  at about 0.95 AU, and, finally,  $3.2 \times 10^5$  at 1.4 AU. The estimate at about 1 AU is in good agreement with the value of  $2.3 \times 10^5$  provided by Matthaeus et al. (2005) on the basis of Equation (3), using simultaneous measurements of interplanetary magnetic field from the *Wind*, *ACE*, and *Cluster* spacecraft, to calculate the correlation length and Taylor scale. Hence, these results show, for the first time in literature, that the effective magnetic Reynolds number increases with the heliocentric distance, clearly indicating that the fast wind becomes more and more turbulent during its expansion.

In the context of an evolving turbulence within fast wind toward a more turbulent state, the results presented in the previous section on the magnetic polarization, compression, and intermittency have to be discussed in the light of drawing a picture of how the left- and right-handed polarized magnetic fluctuations near the proton inertial length evolve as the wind expands.

The populations around the Doppler-shifted ion-cyclotron frequency of magnetic fluctuations with positive and negative helicity, localized at  $\theta_{\text{VB}} \sim 180^\circ$  and  $\sim 90^\circ$ , respectively (Figure 2), are consistent with left-handed polarized Alfvén/ion-cyclotron waves outward propagating quasi-antiparallel to the local magnetic field, and with a spectrum of highly obliquely propagating right-handed KAWs. This last population is characterized by a dominant negative magnetic helicity signature that covers up the presence of Alfvén/ion-cyclotron waves if the spectral analysis is based on the usual Fourier transform techniques (see also He et al. 2011; Podesta & Gary 2011). As a matter of fact, notwithstanding the criticism reported by He et al. (2011) about the limitations of an analysis based on the reduced magnetic helicity, which mostly reveals the helicity of waves propagating quasi-(anti-)parallel to the

radial direction when compared to other waves with similar amplitude but propagating at large angles, if there were no Alfvén/ion-cyclotron waves propagating antiparallel to the local field, it would be difficult to justify the  $\sigma_m$  signature observed around  $180^\circ$ .

Moreover, it has been shown that both these wave families are found at frequencies right after the spectral break separating fluid and kinetic regimes, suggesting that the change in the spectral slope happens to coincide with the low-frequency extent of KAWs and Alfvén/ion-cyclotron waves. Finally, the intermittency analysis shows that the decrease of the flatness begins at the lowest frequencies influenced by the presence of KAWs and Alfvén/ion-cyclotron waves. Unfortunately, the noise level influencing the fluxgate magnetometer data does not allow a reliable investigation of the flatness at frequencies higher than a few hertz. However, there are observational results indicating that, after a noticeable decrease at scales around and smaller than the local proton scales, the flatness exhibits a modest increase toward electron scales (Alexandrova et al. 2008; Wu et al. 2013). Thus, the transition of the flatness back to near-Gaussian values would seem to happen at those frequencies where the stochastic KAWs and the Alfvén/ion-cyclotron waves populate the spectrum. On the other hand, the reported further growth of the flatness would indicate that the higher-frequency extent of both wave populations is dominated by the presence of coherent structures generated by some mechanism acting at kinetic scales (see Wu et al. 2013, and references therein).

The results presented so far on the KAWs and Alfvén/ion-cyclotron waves, such as their spectral extension roughly corresponding to the frequencies right after the spectral break (which coincides with the ion-cyclotron resonance scale) and before the steepening of the spectrum, their frequency shift toward lower values as the wind expands according to the radial evolution of the spectral break, and the role that it would play in the intermittency decrease in the fast solar wind at ion scales, are all pointing to a likely association with some physical mechanisms governing their generation and dissipation to heat the plasma at proton scales, which would be reflected in a change of the scaling exponent.

In summary, the Alfvén/ion-cyclotron waves are less compressive than KAWs, which indeed represent the energetically dominant magnetic fluctuations. However, there is a tendency toward a more balanced energy state between these two kinds of waves, since the power associated with the KAWs decreases more quickly with the heliocentric distance with respect to the Alfvén/ion-cyclotron wave counterpart, in agreement with the expectations that  $k_\perp$  contribute to the turbulence cascade more efficiently than  $k_\parallel$ .

## 5. CONCLUSIONS

*Messenger–Wind* radial alignment is exploited to investigate the radial evolution of the magnetic field fluctuations at proton scales, within the fast wind. The analysis of the distribution of the normalized magnetic helicity spectrum as a function of the angle between the local mean magnetic field and the flow direction of the solar wind allows the identification of two different wave populations, both at frequencies right beyond the location of the spectral break marking the beginning of the region where kinetic effects must be considered. Right-handed polarized KAWs are found

to propagate highly obliquely with respect to the local magnetic field, while left-handed polarized Alfvén/ion-cyclotron waves are observed to propagate at quasi-antiparallel directions. KAWs, which mostly contribute to the overall energy content of the magnetic fluctuations, are largely more compressive than Alfvén/ion-cyclotron waves, though this predominance tends to decrease with distance. On the other hand, Alfvén/ion-cyclotron waves are mainly dominated by directional fluctuations and keep a rough constant compressibility level between *Messenger* and *Wind* locations. As the spectral break moves to lower frequencies during the wind expansion (Bruno & Trenchi 2014), both KAWs and Alfvén/ion-cyclotron waves shift accordingly to lower frequencies, which, per se, is an experimental evidence that strongly relates the location of the frequency break to the presence of these fluctuations. Furthermore, the stochastic nature of these fluctuations might also be strongly related to the observed depletion of intermittency just before the frequency break. These observational evidences firmly point to a clear association of the frequency region where KAWs and Alfvén/ion-cyclotron waves are found with the high-frequency break location and, in turn, with the change of the spectral slope, which would support some form of dissipation, as ion-cyclotron resonance and Landau damping, of the energy transferred along the inertial range.

In this context and in light of the recent findings by Bruno et al. (2014), it would be worth characterizing these fluctuations moving from fast- to slow-wind regions, to further investigate the response of the dissipation mechanism to the level of the energy carried by the waves. However, this is beyond the purpose of this paper and will be devoted to a future work in preparation.

This research was partially supported by the Italian Space Agency (ASI) under contracts I/013/12/0 and I/022/10/2 and by the European Commission's Seventh Framework Program under the grant agreement STORM (project n° 313038). Data from *Wind* and *Messenger* were obtained from NASA-CDAWeb and NASA-PDS websites, respectively.

## REFERENCES

- Alexandrova, O., Carbone, V., Veltri, P., & Sorriso-Valvo, L. 2008, *ApJ*, **674**, 1153
- Alexandrova, O., Chen, C. H. K., Sorriso-Valvo, L., Horbury, T. S., & Bale, S. D. 2013, *SSRv*, **178**, 101
- Anderson, B. J., Acuña, M. H., Lohr, D. A., et al. 2007, *SSRv*, **131**, 417
- Bavassano, B., Dobrowolny, M., Fanfoni, G., Mariani, F., & Ness, N. F. 1982, *SoPh*, **78**, 373
- Bourouaine, S., Alexandrova, O., Marsch, E., & Maksimovic, M. 2012, *ApJ*, **749**, 102
- Bruno, R., & Bavassano, B. 1991, *JGR*, **96**, 7841
- Bruno, R., & Carbone, V. 2013, *LRSP*, **10**, 2
- Bruno, R., Carbone, V., Sorriso-Valvo, L., & Bavassano, B. 2003, *JGR*, **108**, 1130
- Bruno, R., Pietropaolo, E., Servidio, S., et al. 2008, AGU Fall Meeting, SH42A-06
- Bruno, R., Telloni, D., Primavera, L., et al. 2014a, *ApJ*, **786**, 53
- Bruno, R., & Trenchi, L. 2014a, *ApJL*, **787**, L24
- Bruno, R., Trenchi, L., & Telloni, D. 2014b, *ApJL*, **793**, L15
- Dmitruk, P., et al. 2004, *ApJ*, **617**, 667
- Galtier, S. 2006, *JPIPh*, **72**, 721
- Gilman, D. L., Fuglister, F. J., & Mitchell, J. M., Jr. 1963, *JAtS*, **20**, 182
- Goldstein, M. L., Roberts, D. A., & Fitch, C. A. 1994, *JGR*, **99**, 11519
- Hamilton, K., Smith, C. W., Vasquez, B. J., & Leamon, R. J. 2008, *JGR*, **113**, A01106
- He, J., Marsch, E., Tu, C., Yao, S., & Tian, H. 2011, *ApJ*, **731**, 85
- He, J., Tu, C., Marsch, E., & Yao, S. 2012a, *ApJ*, **749**, 86
- He, J., Tu, C., Marsch, E., & Yao, S. 2012b, *ApJL*, **745**, L8
- Horbury, T. S., Forman, M., & Oughton, S. 2008, *PhRvL*, **101**, 175005
- Jenkins, G. M., & Watts, D. G. 1968, *Spectral Analysis and Its Applications* (San Francisco, CA: Holden-Day)
- Leamon, R. J., Smith, C. W., Ness, N. F., Matthaeus, W. H., & Wong, H. K. 1998, *JGR*, **103**, 4775
- Lepping, R. P., Acuña, M. H., Burlaga, L. H., et al. 1995, *SSRv*, **71**, 207
- Markovskii, S. A., Vasquez, B. J., & Smith, C. W. 2008, *ApJ*, **675**, 1576
- Marsch, E. 2012, *SSRv*, **172**, 23
- Matthaeus, W. H., Dasso, S., Weygand, J. M., et al. 2005, *PhRvL*, **95**, 231101
- Matthaeus, W. H., & Goldstein, M. L. 1982, *JGR*, **87**, 6011
- Matthaeus, W. H., Goldstein, M. L., & Smith, C. 1982, *PhRvL*, **48**, 1256
- Percival, D. P. 1995, *Biometrika*, **82**, 619
- Perri, S., Carbone, V., & Veltri, P. 2010, *ApJL*, **725**, L52
- Podesta, J. J., & Gary, S. P. 2011, *ApJ*, **734**, 15
- Sahraoui, F., Goldstein, M. L., Robert, P., & Khotyaintsev, Yu. V. 2009, *PhRvL*, **102**, 231102
- Taylor, G. I. 1938, *RSPSA*, **164**, 476
- Torrence, C., & Compo, G. P. 1998, *BAMS*, **79**, 61
- Tu, C. Y., & Marsch, E. 1995, *SSRv*, **73**, 1
- Wu, P., Perri, S., Osman, K., et al. 2013, *ApJL*, **763**, L30